Synchrotron quantification of graphite nodule evolution during the solidification of cast iron

Azeem, M.A.; Bjerre, M. K.; Atwood, R.C.; Tiedje, N.; Lee, P. D.

Published in:
Acta Materialia

Link to article, DOI:
10.1016/j.actamat.2018.06.007

Publication date:
2018

Document Version
Publisher's PDF, also known as Version of record

Acta Materialia 155 (2018) 393–401

Contents lists available at ScienceDirect

Acta Materialia

journal homepage: www.elsevier.com/locate/actamat

Full length article

Synchrotron quantification of graphite nodule evolution during the solidification of cast iron

M.A. Azeem [a, b], M.K. Bjerre [c], R.C. Atwood [b, d], N. Tiedje [c, **], P.D. Lee [a, b, *]

[a] Mechanical Engineering, University College London, London, WC1E 7JE, UK
[b] Research Complex at Harwell, RAL, Didcot, OX11 0FA, UK
[c] Department of Mechanical Engineering, Technical University of Denmark, DK-2800 Kgs, Lyngby, Denmark
[d] Diamond Light Source Ltd., Harwell Science and Innovation Campus, Didcot, OX11 0DE, UK

ARTICLE INFO

Article history:
Received 18 March 2018
Received in revised form
24 May 2018
Accepted 2 June 2018
Available online 13 June 2018

Keywords:
Graphite morphology
Cast iron
Synchrotron radiation computed tomography
Nucleation and growth
Growth kinetics

ABSTRACT

In cast iron, graphite develops in conjunction with the metallic matrix during solidification. The morphology and distribution of the embedded graphite is pivotal for mechanical properties from yield strength to fatigue. A novel high temperature environmental cell was developed and combined with *in situ* synchrotron tomography to investigate and quantify microstructural evolution, including graphite nodule nucleation and growth rates in ductile cast iron. The mechanisms of degenerate graphite nodule formation were also revealed. The formation of a coherent primary gamma phase dendritic network before the graphite nucleation is demonstrated. The graphite nodule nucleation rate, mobility and growth rates are compared to classical models, highlighting the limitations in these models. The results provide unique insights to tune the temperature pathways during cast iron solidification to achieve desired uniform rounded graphite morphologies and size distributions.

1. Introduction

Cast iron, with its wide range of graphite forms, excellent castability, and range of properties has been the most widely used metal in cast form for centuries. The continued use of cast iron is due to increasing demand from the renewable energy and maritime sectors, as well as heavy equipment manufacturing [1]. The graphite phases in cast iron(s) develops in conjunction with the metallic matrix during solidification – understanding and controlling their structure, number density and morphology is key to cast iron's properties.

Although many high strength alloys from steels to Ni superalloys are currently strengthened by carbon additions via the formation of nano to micron-sized carbides, very few alloys other than cast irons, based on the Fe-C system with >2 wt% carbon, use the formation of graphite to provide ease of melt processing coupled with high strength and fatigue properties. The size, distribution, crystallography and shape of the graphite particles can be controlled by changing the solidification pathways and by addition of modifying elements such as Mg [2], Ti [3], Ce etc. The resulting composites are referred to by different names depending on their mechanical properties, morphology of the graphite particles, properties or appearance (for example grey, nodular/ductile).

One form is nodular cast iron, named for the spherical shape of the graphite phase. Cast irons have exceptional stiffness, better than that of Al, Mg and Ti alloys [4–6]. The excellent castability of cast iron, in combination with the high damping capacity of the graphite phase make cast irons a material of choice for complex shaped components exposed to vibration and fatigue loading.

The damping capacity reduces as the graphite features become more rounded; therefore, cast irons with flaky graphite have much greater damping capacity than those with spherical graphite; however, the ductility of spherical graphite cast irons is higher. Complex structures with dynamic load bearing capacity, such as wind turbines [1], automotive engines, maritime drive systems and hydroelectric power systems, benefit from the balance of these properties provided by nodular cast iron. Unfortunately, finding the processing route for reliably obtaining uniform spherical nodules has been difficult for solidification at low cooling rates and the mechanisms behind the shape development have previously not been observed.

* Corresponding author. Research Complex at Harwell, RAL, Didcot, OX11 0FA, UK.
** Corresponding author. Technical University of Denmark, Lyngby, Denmark.
E-mail addresses: nsti@mek.dtu.dk (N. Tiedje), peter.lee@ucl.ac.uk (P.D. Lee).

https://doi.org/10.1016/j.actamat.2018.06.007

Globally, the combined share of cast irons by tonnage is the highest of all metal castings used [7]. Thus cast irons, which are easily recyclable, play a key technological role whilst having a low impact on the environment during the full life cycle of the components.

The graphite nodules and their distribution in nodular cast irons almost entirely dictate the mechanical response of the composite microstructures. In the absence of modifying agents, the graphite grows in a flaky fashion, reducing ductility [8]. Methods for transforming the flaky morphology into spherical nodules during solidification were first identified in the mid-20th century [9] and ever since, empirically established methods to improve the morphology have been developed [10–12]. During eutectic solidification, the graphite nodules are encapsulated in an austenite (γ-Fe) shell, which develops from pre-existing austenite dendrites or nucleates on the surface of the graphite. This shell isolates the nodule from liquid; the resulting flow of carbon is limited by diffusion through the shell wall and thus maintains the spherical morphology of the encapsulated nodule. However, several researchers have observed that a significant proportion of nodules in industrial castings are not spherical, they are observed to develop distinct peripheral extensions [2,13,14], and other degenerate morphologies [15]. These variant graphite morphologies appear during nominally identical thermal conditions, highlighting our lack of fundamental understanding of the nucleation and growth kinetics of carbon phases emerging from molten metallic melts during freezing.

In this investigation, we combine *in situ* synchrotron tomography, a novel high temperature environmental cell, and a bespoke encapsulation technique to reveal the previously hidden nucleation and growth mechanisms. Real-time nucleation of graphite, growth, their respective rates, size distribution and interaction between the nodule and the shell are systematically captured and evaluated. The results provide essential information that may be used to tune temperature pathways during solidification of metal-carbon composites in order to achieve uniform rounded morphologies and desired size distribution.

These observations would not have been possible without the availability of advanced *in situ* X-ray imaging facilities. *In situ* X-ray radiography (2D plus time) [16] and tomography (4D, 3D plus time) [17–20] have been used before to capture nucleation, growth and evolution of metallic microstructural features ranging from a few microns to several hundreds of microns. The technique was recently used to capture the formation of graphite in a Mg modified hypereutectic iron-carbon alloy [21]. Radiography may be performed at higher speed, capturing fast evolving features, but due to constraining 2D geometries it may not be representative of the bulk behaviour. Third generation synchrotron sources allowed fast 4D (3D + time/stress/temperature) tomography, they were used to investigate low temperature metallic alloys as they solidify [18,19], up to 700 °C, informing and validating models developed for predicting dendritic microstructures [22–25] and defects in metals [26].

Using the combination of a novel bespoke high temperature environmental cell enabling temperatures up to 1500 °C [17] and a methodology to contain cast iron in an X-ray transparent module at temperatures exceeding 1000 °C, we have performed the first 4D imaging of graphite formation in a high temperature alloy, cast iron.

2. Methods

The composition of the cast iron alloy used in this investigation is provided in Table 1, Mg was added to promote the formation of regular spherical nodules. The synchrotron X-ray tomography experiment was performed at the I12 beamline [27] of the Diamond Light Source, UK. A schematic of the beamline set-up and the sample module used in this investigation is shown in Fig. 1a and b respectively. The experiment was performed on a Ø 2 × 8 mm tall cylindrical specimens, encapsulated in a ~2.1 mm internal diameter quartz tube tapered at the top to pinch the specimen. A glass rod was used to hold the sample at one end of the ~25 mm tall encapsulated tube to prevent it from moving during the course of solidification. This arrangement provided an X-ray imaging set up with very little contact between the specimen and the quartz crucible, (see Supplementary Fig. S1 and movie M1), thus minimizing the reaction between the cast iron and the quartz. The reaction between the crucible and enclosed sample was further minimized by holding the alloy for only a few seconds in the molten state, as shown in the temperature profile in Supplementary Fig. S2.

Supplementary video related to this article can be found at https://doi.org/10.1016/j.actamat.2018.06.007.

The assembly was mounted on an alumina ceramic ram and the heating was performed using a bespoke environmental cell. The design details of the environmental cell and sample module are provided elsewhere [17]. During tomography experiment, the sample was first heated to 1167 ± 0.5 °C at a rate of 0.5 °Cs^{-1}, briefly held in liquid state and then cooled at a rate of 0.03 °Cs^{-1}. Tomographic acquisition was performed using a 70 keV monochromatic beam. In total, 62 tomograms were acquired with 360 projections per tomogram and exposure time of 0.11 s was used per projection (or 40 s per tomogram). Algorithms previously published by Raven [28] and Paganin et al. [29] were used for ring removal, and to enhance the contrast of the 2D projections respectively, before using filtered back-projection for reconstruction.

3. Results and discussion

The chemistry of the alloy used in this investigation is specifically chosen such that the formation of nodules is promoted. It consists of ~2 and 0.07 wt% Si and Mg respectively, Si stabilizes the graphite [12] and Mg promotes the formation of nodules [11,12,15]. The multitude of graphite morphologies revealed at high temperature just after solidification by the in situ setup is shown in Fig. 2a. The dark phase in the 2D superimposed *XY*, *XZ* and *YZ* slices are (solid) graphite and the bright region is comprised of liquid and solid austenite dendrites, they are indistinguishable due to similar X-ray attenuation. The outer, region of this Ø 2 mm cylindrical specimen contains compacted graphite (also known as vermicular graphite), it is a variant of flaky graphite with thicker features and blunt tips. In a metallic matrix, the presence of sharp incoherent features reduces ductility as a result of accelerated crack initiation in the matrix during mechanical loading. The diverse graphite morphologies in the entire 8 mm tall specimen are shown in Fig. 2b.

The overview image provided in Fig. 2b shows the final graphite morphology through the entire sample after it has solidified. The central region of the sample is nodular graphite (see Fig. 2a). However, there is a thin peripheral region where compacted graphite has formed. This is due to the loss of Mg from the exterior of the sample to the inert atmosphere in the capsule, depleting the Mg level for a few hundred microns from the sample edge. As shown in supplementary movie M1, the graphite forms first in the thin peripheral region via the nucleation of compacted graphite and austenite dendrite (γ). The growth morphology of the dendrites is governed by constitutional undercooling resulting from

Table 1
Composition (in wt. %) of the cast iron alloy used.

C	Si	Mg	P	Cu	Mn	S
3.6	1.91	0.075	0.017	0.012	0.099	0.001

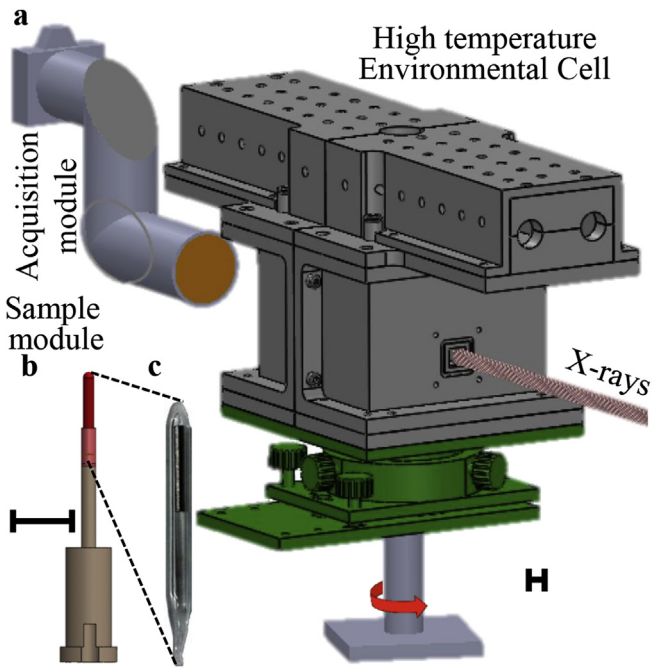

Fig. 1. (a) schematic of the environmental cell setup at the I12 beamline of Diamond Light Source, (b) Schematic of the sample module with alumina sample mount and quartz encapsulated sample and (c) image of the as-encapsulated sample, held in place at one end of the encapsulation by a quartz rod. Scale bar = 20 mm.

partitioning of solute elements, including carbon to the adjacent liquid. The distribution of Si, partitioning into the growing dendrites, is shown in a large area EDX map in Supplementary Fig. S3, revealing the austenite's dendritic structure. The austenite primary phase nucleates on the sample walls, with columnar dendrites growing inwards, followed by development of equiaxed dendrites in the interior volume.

As solidification progresses, nodular graphite nucleates (see Fig. 2c) in the large central region (where Mg is not depleted) and the growth of compacted graphite ceases. The thin Mg depleted zone is excluded from the analysis below, to focus on nodular graphite formation.

We reveal the first 4D observation of the graphite nucleation and evolution of nodules, as shown in Fig. 2c–f and supplementary movie M2. The graphite nodules nucleate in the solute-enriched liquid, enrichment that happens by the rejection of solute from the growth of γ dendrites. The Mg is retained in the central volume, facilitating spherical morphology development. The nodules start to nucleate at $1130 \pm 0.5\,^{\circ}C$ and the growth plateaus at $1124 \pm 0.5\,^{\circ}C$. During this temperature interval 7 tomograms were acquired. Graphite nodules were observed to nucleate during the entire thermal interval. The size distribution of nodules at different times during solidification is shown in Supplementary Fig. S4.

Supplementary video related to this article can be found at https://doi.org/10.1016/j.actamat.2018.06.007.

Current literature disputes many key aspects of nodule formation, their nucleation, growth kinetics, with the formation of degenerate features. Our 4D imaging results resolve these long-standing debates. In the central volume, the development of about 1000 nodules (regular and degenerate) is captured. All the nodules, except a few (<0.5%), remain fixed during the course of solidification, as shown in Fig. 2c–f and supplementary movie M2. This is only possible if the nodules are attached to or held in place by stable microstructural features such as the γ-dendrites during nucleation and growth, otherwise their large density difference with the surrounding liquid iron would cause them to quickly float upwards.

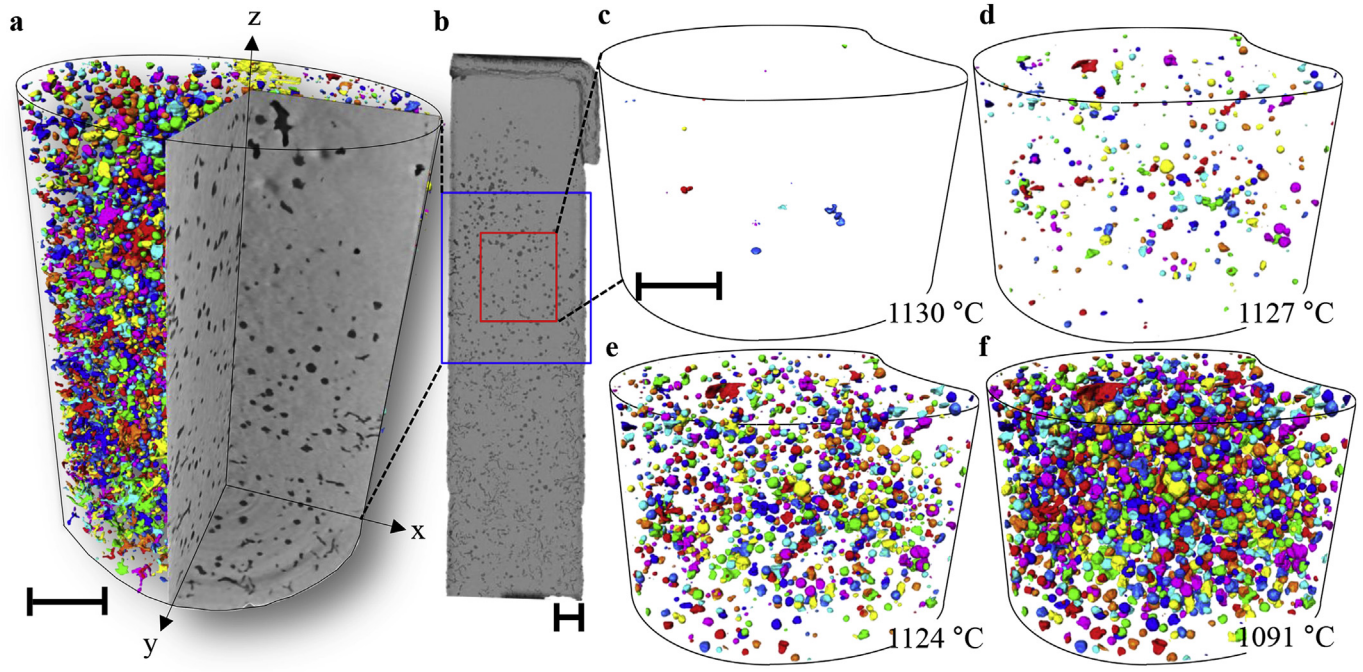

Fig. 2. Tomography images revealing (a) multitude of graphite morphologies observed in 3D after solidification in a 3 × 2 mm field of view, (b) the post-solidification graphite morphologies in the entire 8 mm sample at room temperature, a montage of 2D slices extracted from five high resolution *ex situ* tomograms, the region of the sample in which *in situ* observations were performed as shown in (a) is highlighted by a blue rectangle. Red highlights a sub-volume, the central region where predominantly nodular graphite morphologies were observed. The evolution of graphite nodules in the central volume is shown in 3D in (c)–(f), corresponding to a temperature range of 33 °C. The evolution of graphite in the 3 mm tall FOV is shown in 2D in supplementary movie M1. Scale bar = 300 μm. (For interpretation of the references to colour in this figure legend, the reader is referred to the Web version of this article.)

We hypothesize that prior to nucleation of nodules, a coherent web of dendrites is formed. The inter-dendritic regions and regions between the secondary dendritic arms are C enriched (as depicted in phase diagram Supplementary Fig. S5), providing ideal locations for nodules to nucleate. Selective nucleation of nodules in the vicinity of dendritic arms was observed in a recent *in situ* radiographic investigation on a Mg modified cast iron alloys [21].

Nucleation of nodules: The formation of graphite nodules commences either by homogeneous nucleation via very large undercooling [30] or through heterogeneous nucleation on inclusions. In Fe-C melts, the heterogeneous nuclei are believed to be oxides or sulphide inclusions, for example, MgO or MgS in a purely Mg treated alloy [13]. We observed distinct Mg inclusion (see Fig. 3) at the core of many nodules, demonstrating MgO/MgS assisted heterogeneous nucleation to be the most likely nucleation mechanism. The presence of Mg in the specimen was also confirmed using time of flight secondary ion mass spectroscopy (TOF-SIMS), as detailed in supplementary note 1 and Supplementary Fig. S6.

Development of regular nodules: Immediately after nucleation, the graphite particle has uninterrupted access to carbon rich liquid. The graphite tends to grow isotropically, even though the surface energy for growth along non-basal crystallographic systems is much larger than that of the basal system [30,31]. There are two mechanisms proposed for isotropic growth. Firstly, equally preferential growth along basal and non-basal systems, which can be feasible as a result of large undercooling[30] with respect to graphite liquidus. Secondly, in a recent investigation [32], stacking fault assisted curved growth along basal slip is identified as a prominent mechanism. After the isotropic stage, the following growth is polycrystalline; the grains grow with their basal planes radially aligned. These two stages of growth are clearly evident from the internal microstructure of the graphite (Supplementary Fig. S7). This matches with recent investigations [15,30,33] which showed that the growth of graphite from metallic melts advances in stages where the internal structure is compartmentalized [30] into three distinct zones, the core comprising of isotropically grown graphite (Stage SI) followed by a zone of concentric graphene rings (SII), often referred to as cabbage structure[14] on top of which close packed conical grains grow radially (SIII).

Formation of graphite consumes carbon from the surrounding liquid, either triggering austenite nucleation in vicinity or accelerating the growth of any surrounding austenite. The austenite engulfs the entire nodule and forms a shell with a typical shell radius of 2.3 times the nodule radius [34]. In the case of unanchored nodules, encapsulation increases the density, thus reducing their buoyant ascent to the top. However, in the current specimen, > 99.5% of nodules remain anchored from nucleation until the end of solidification. A significant proportion of nodules are observed to develop degenerate features. For the first time we observe the mechanisms and stages by which these features form.

Development of degenerate nodule morphologies: The growth of regular and degenerate nodules in a magnified subvolume is shown in 3D in Fig. 4a–d and supplementary movie M3. The nodules are classified into regular and degenerate, based on sphericity (Ψ), a measure of roundness. Nodules with $\Psi > 0.75$ are classified as regular and the remaining as degenerate. (Note: The classification criterion is elaborated further in supplementary note 2). Strikingly, all the degenerate nodules are spherical in the beginning; then the degenerate features emerge from them spontaneously later on during solidification. For example, the formation of a "polyp-like" extension (indicated by red arrows in Fig. 4b) and the formation of spherical blobs at the free ends of these polyps appear within two consecutive tomograms, 40 s apart and corresponding to a temperature difference of 1 °C.

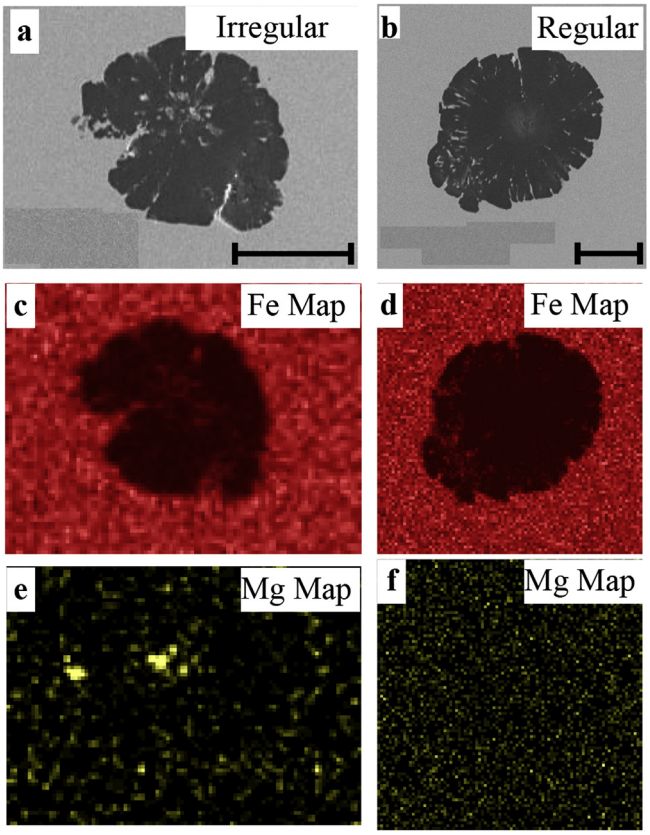

Fig. 3. Nodule internal structure after (a) nucleation on large oxide particle (b) nucleation on relatively much finer particle or via homogeneous nucleation. The distribution of Fe in the corresponding region is shown in EDS maps (c) and (d) respectively. The distribution of Mg in the corresponding region is shown in (e) and (f) respectively. Scale bar = 20 μm.

Supplementary video related to this article can be found at https://doi.org/10.1016/j.actamat.2018.06.007.

The in-place growth of nodules, as evident from Fig. 2c–f and supplementary movie M2, suggests that formation and growth happens between the secondary arms or interdendritic space. (Note that the imaging resolution in the experiment was ~5 μm, thus, flotation at smaller length scales than this would not have been captured). This is also evident from the SEM EDS maps of the Si (Supplementary Fig. S3), where the nodules are confined to interdendritic space or remain at the periphery of γ-iron dendrites.

The formation of an intact austenite shell detaches the enclosed nodules from a direct supply of carbon. The following growth of the nodule is therefore regulated by diffusion of carbon through the austenite shell. Due to diffusion the carbon equilibrates across the nodule thus normalizing the growth rate of individual radial grains (Stage III of nodule growth[14]). As solidification continues, γ-iron continues to form, increasing the carbon concentration in the interdendritic liquid, causing more carbon to diffuse through the shell wall. The resulting graphite growth exerts an increasingly higher force, creating a high stress in the shell. Existing models of spheroidal growth mostly stop here. However, as mentioned in the introduction, protrusions (polyps) from spherical nodules are frequently observed. Our results (Fig. 4a–d and supplementary movie M3) reveal how these polyps form.

Following a nodule's growth through time, we see N3 (Fig. 4a) initially grows in a spherical fashion (Supplementary movie M3), almost certainly surrounded by an austenite shell. In Fig. 4b, we see an all-new development, how the polyp forms via extension through a crack in the shell, subsequently growing into the carbon

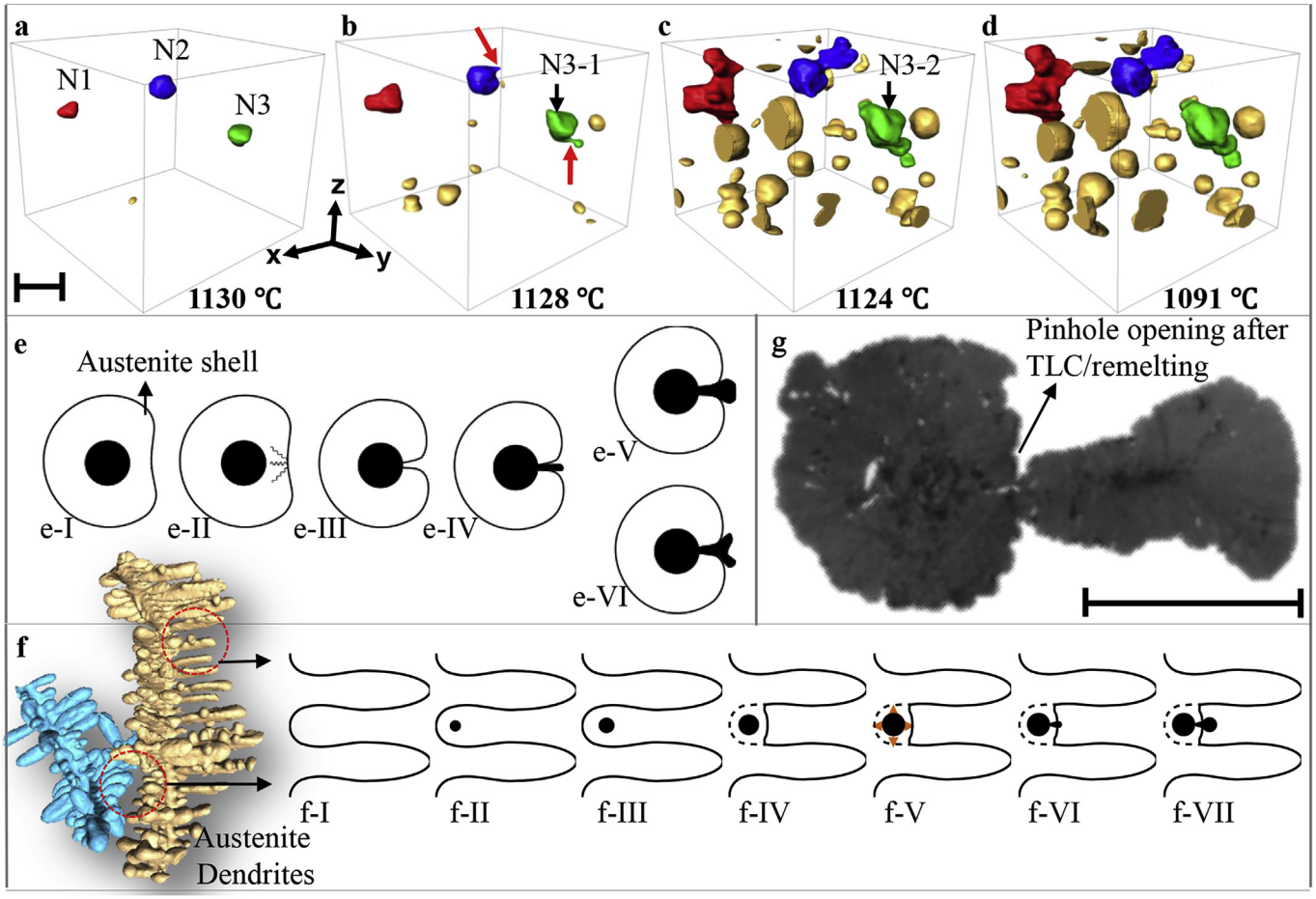

Fig. 4. : (a)–(d) 4D (3D + time) plese shell, rupturing it via creep of the austenite, dissolving the austenite, or cracking the shell due to the applied stress. *In situ* data capturing the evolution of nodules in a sub-volume taken from the central region of the specimen. Three irregular nodules, N1 (red), N2 (blue) and N3 (green) have been emphasized to demonstrate the various stages involved in the development of degenerated features. Initially, the nodules assume a spherical morphology, as shown in (a). Then, the degenerated features start to appear via formation of polyps, as indicated by red arrows in (b). On the ends of the polyps, more features develop during later stages of solidification, as shown in (c) and (d). The two mechanisms of formation of degenerated morphologies are schematically shown in (e) and (f) respectively. The morphology of bead-like growth in nodule N3 examined at room temperature using an optical microscope is shown in (g). Scale bar = 50 μm. (For interpretation of the references to colour in this figure legend, the reader is referred to the Web version of this article.)

enriched liquid, a spherical cap (N3-1) redevelops, temporarily arresting its forward growth. In Fig. 4c, we see development of a second polyp, from the first, again forming a spherical cap (N3-2). The mechanisms of formation of these degenerate morphologies are hypothesised below.

The formation of degenerate features in unanchored nodules is schematically depicted in Fig. 4e. The austenite shell is either single [34] or poly crystalline [35], depending on the nucleation of austenite in vicinity of the nodule. In order for the encapsulated nodules to develop degenerate features, the graphite has to grow through the austenite shell, via, (1) creep rupturing of the austenite shell, (2) dissolution of austenite or (3) by cracking of the shell due to stresses. Creep deformation and failure by cavitation, possibly accelerated by fast diffusion of interstitial carbon and other atomic entities including vacancies could be one of the mechanisms of disintegration. However, creep is a relatively slow damage mechanism where dislocations move over long periods – here the growth of the polyp happens in a single tomographic frame (i.e. in seconds). Dissolution of the austenite is unlikely as the temperature is continuously reducing, making it ever more stable. Therefore we hypothesize that a cracking mechanism is the most likely.

Recently, transgranular liquation cracking (TLC) has been identified as a prominent grain fragmentation mechanism in FCC metals [36], where, brittle-like cracking was observed to occur in large AlCu grains subjected to point loading during indentation in the semi-solid state. The shell is subjected to tensile stresses from the growing nodule, as depicted in Fig. 4e(e-II). We hypothesize that the high strain in the shell locally increases the free energy, reducing the melting temperature, and a surface dimple in the shell forms which combined with dislocations, vacancies and high diffusivity of interstitials causes liquid assisted cracking, similar to brittle-like cracking as that observed in single crystals of AlCu [36]. The graphite grains in the nodule grow through the ruptured shell (Fig. 4e(e-III)). This transgranular or intergranular liquation cracking of the shell exposes a few radially growing conical grains to the carbon-rich liquid metal. The exposed grains grow through the opening and appear like a polyp. This mechanisms could also explain the rupturing of austenite shell during the development of cabbage structure in stage SII of growth, as has been previously reported in as-quenched cast iron micrographs [37]. Subsequently, a second γ-Fe shell develops around the polyp and the tip of the polyp assumes a rounded morphology.

The proposed mechanism of formation of degenerate morphologies in anchored nodules is schematically illustrated in Fig. 4f. Here, the graphite nodule is encapsulated by the growth of the anchoring dendrite(s). During post encapsulation growth, the load

distribution in the encapsulation is uneven due to varying shell thickness. Naturally, thinner sections of the shell undergo largest strain leading to cracking, again we propose by TLC. In the case of degenerate nodule N3 (Fig. 4c), the length of the polyp was found to be ~50 μm, which corresponds to the widely reported shell to nodule radius ratio of 2.3 [34]. At the free end of the polyp, a spherical graphite bulb develops most likely due to formation of a γ-Fe shell. A second polyp along the same polyp axis as previous appears when the new γ-Fe shell cracks, resulting in a bead-like morphology, Fig. 4c and d. In contrast, the polyp in N2 splits (possibly assisted by crystal defects such as twins [15,32,38]) into three branches and eventually a spherical graphite bulb develops with an associated γ-Fe shell at the end of each polyp during further cooling. These morphological observations were confirmed through post-solidification optical microscopy. An optical micrograph of a slice through the nodule N3 is shown in Fig. 4g. Clearly, the segments of the bead are bridged by coherent polyps growing through the pinhole formed by remelting/cracking. This new understanding provides inputs for advancing mold design in order to optimize the temperature and pressure in large metal-carbon castings for achieving spherical nodules.

The real-time 3D observations presented here reveal key developmental steps involved in the formation of degenerate features on the nodular graphite answering the long debated hypothesis of the underlying mechanisms. The observations are generating new insights into the rupturing of the austenite shell, the rapid development of polyps, their branching, and the development of bead-like and branched morphologies. These are of practical significance with regards to the vast dependence of our engineering industry on cast irons, and the potential applications of metal-carbon alloys.

Nucleation and growth kinetics: Our 4D images allow us to not only investigate mechanisms, but also, for the first time, to study the nucleation and growth characteristics of regular and degenerate nodules in unprecedented detail. This is critical for engineering applications where the response of a composite microstructure to external stresses can depend on the size distribution of the graphite phase. Prediction of the final size distribution

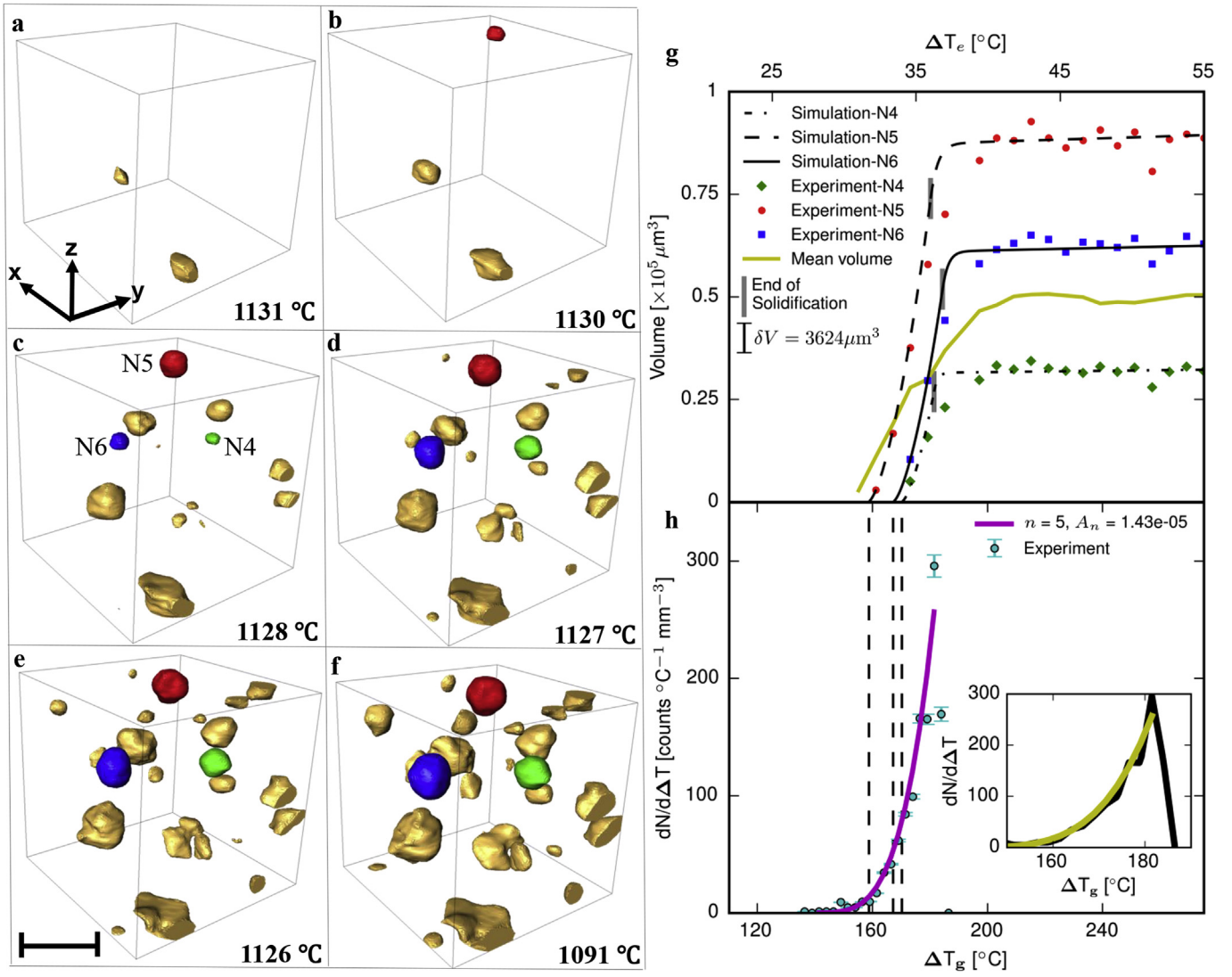

Fig. 5. The evolution of nodules in a sub-volume of the specimen captured using *in situ* synchrotron X-ray tomography is shown in (a)–(f). Three regular nodules, N4 (green), N5 (red) and N6 (blue) are emphasized and their growth during the course of solidification is shown in (g) as a function of undercooling with respect to graphite liquidus (ΔT_g) and the eutectic temperature (ΔT_e, provided on secondary X-axis). The three nodules nucleate and grow to their maximum size within a temperature range of 6 °C. The evolution of mean size of the particles within this volume is also provided for comparison. The observed and modelled nuclei distribution per unit volume of the specimen as a function of undercooling is provided in (h). Scale bar = 100 μm. (For interpretation of the references to colour in this figure legend, the reader is referred to the Web version of this article.)

is essential to predict final component strength and measurement of nucleation and growth kinetics of the nodules during solidification is essential to inform and validate models. Using three regular nodules, N4 (green), N5 (red) and N6 (blue), we demonstrate the process of quantifying nucleation and growth kinetics (Fig. 5).

The volumetric growth (V) of the regular nodules N4, N5 and N6 as a function of cooling below with respect to graphite liquidus, ΔT_g (= Graphite liquidus temperature (T_{gl}) − specimen temperature (T)), is shown in Fig. 5g. T_{gl} is obtained from the phase diagram using the temperature of the sample and assuming that the liquid is in equilibrium with austenite. This requires estimation of carbon content at T, which is detailed in supplementary note 3. Essentially, it involves estimation of instantaneous carbon content in the solid phases, i.e., the carbon in the form of graphite and the carbon concentration of austenite. The latter is estimated by evaluating the fraction of austenite via the lever rule, assuming that the Si remains uniformly distributed during the course of solidification. The extent of undercooling is illustrated in Supplementary Fig. S5.

The nodules that nucleated earlier during the course of solidification are generally the largest at the end of solidification. For example, nodule N4, which nucleates at 1130 °C ($\Delta T_g = 156$ °C) is the largest nodule in this sub-volume. The mean size of the nodules in this sub-volume is also provided for comparison. Irrespective of nucleation temperature and final size, the growth is seen to plateau at ~1123 °C, when the carbon is completely depleted from the nodule vicinity, or when the nodule is completely isolated from the liquid. A graphite growth model based on Lesoult et al. [39] is used to study the effect of temperature and time on the growth of the three nodules. The encapsulating austenite is assumed to be in local equilibrium with the liquid. The calculation of uncertainty in sizes and the salient aspects of the model are elaborated in supplementary notes 3 and 4 respectively. The predicted growth rate is higher than that observed in stages before the plateau, because the model does not take into consideration the reduction in carbon during later stages.

The nucleation temperature for each graphite nodule is estimated by extrapolating the growth of the nodules back to zero volume, this method has been previously used for evaluating nucleation of porosity [40], intermetallics [41] and other phases. On average, the extrapolation was over a temperature range <1.2 °C, which is also the temperature change during a single tomogram. The measured and predicted rate of nucleation ($dN/d(\Delta T_g)$), i.e., the number of nodules nucleated per change in temperature in a unit volume of liquid in the specimen, as a function of ΔT_g is shown in Fig. 5h and a selected region of interest around the peak rate of nucleation is shown in inset. The nucleation starts at undercooling $\Delta T_g = 156$ °C, it increases rapidly, peaking at a ΔT_g of 180 °C and then declines sharply. The model can be used to predict only the initial nucleation trend due to the fact that nucleation is entirely dependent on the extent of undercooling and does not take into consideration any solute depletion by growing nodules. In reality, the solidification volume available is limited and therefore the nucleation rate starts declining as the remaining liquid volume decreases, and the nodules locally deplete the carbon in that liquid.

Continuous nucleation in ductile cast iron has previously been described by a function of the Oldfield-type [42]: $dN/d(\Delta T_g) = A(\Delta T_g + c)^n$ where A, n and c are constants. Fitting this equation to the experimental data and restricting the power n to integer values, $n = 5$ yields the best fit with an offset from the graphite liquidus temperature of approximately $c = 138$ °C and $A_n = 1.43 \times 10^{-5}$ counts °C^{-1} mm^{-3}. The calculated n is large compared to previously reported results but it corroborates well with the nucleation kinetics observed in low inoculant potency systems [43].

Monitoring the growth rate of individual particles as a function of their size can capture the effect of decreasing liquid volume on the size distribution of graphite in the specimen during solidification. In our *in situ* experiments, we track hundreds of nucleation and growth events, a few of which are shown along with simulated data for regular and degenerate nodules in Fig. 6a and b respectively. The data is taken from four consecutive tomograms, representing a solidification regime spanning 120 s. The volumetric rate change was calculated as follows. Considering a specific nodule with volume V_1 at time t_s and V_2 at time $t_s+\Delta t$ where Δt is the time between scans, in this case 40 s. The growth rate is then calculated as $(V_2\text{-}V_1)/\Delta t$, which is plotted against the average of V_1 and V_2. The nodule growth rate increases initially, peaks and then reduces in later stages of solidification. In order to visually enhance this trend, the data points corresponding to three different (in size) nodules have been connected. Immediately after nucleation, the liquid is supersaturated with carbon, so growth accelerates. As the excess carbon depletes, the growth peaks and slows as the austenite shell forms and grows thicker.

One of the primary assumptions in the model is that the carbon content outside the austenite shell does not change during growth. But in reality it does change, as has been clarified previously. In Fig. 6a, two model predictions are provided, one where the carbon

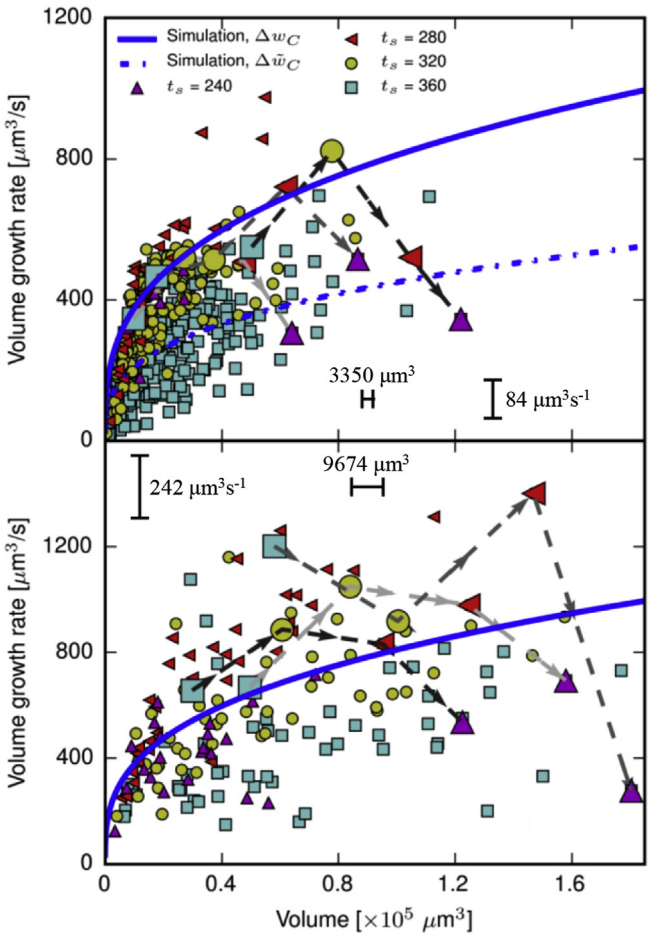

Fig. 6. The observed and predicted graphite growth rate of nodules in a sub-volume during solidification as a function of size is shown here for the case of (a) regular nodules and (b) irregular nodules. The growth rate in both types increases initially and then reduces during culminating stages of solidification, as depicted by connecting the data points of select few (enlarged symbols) nodules by arrows. The predicted behaviour for early (solid blue line) and late (dashed blue line) stages of growth is provided along with mean uncertainties. (For interpretation of the references to colour in this figure legend, the reader is referred to the Web version of this article.)

concentration at the liquid austenite interface is equilibrium concentration taken from the phase diagram, Δw_C, and the other where this concentration is reduced by 0.11 wt%, $\Delta \tilde{w}_C$, the latter representing late stages of solidification. The differences between early and late stage simulations are detailed in supplementary note 5. Again, the model falls short of predicting the behaviour observed in later stages of solidification due to the fact that the solidification conditions are far from the idealized assumptions on which the model is based. Thus the direct high temperature observation of nucleation and growth provides unique insights and establishes a gold standard dataset by which to develop and validate advanced models.

4. Conclusions

This investigation resolves the long-standing debate on the locational preference of nucleation of graphite nodules in the Fe-C alloy system during solidification. The nucleation and growth of nodules is systematically evaluated for the first time using 4D (3D + time) high temperature *in situ* synchrotron X-ray tomography and 1D simulations. It was hypothesized, and verified, that graphite nucleates between dendrite arms; i.e., during solidification, the graphite nodules remain anchored and grow in place. Initially, they are spherical and then the degenerate morphologies develop via a burst growth stage, forming polyp-like features. The mechanisms of formation of these degenerate morphologies via transgranular liquation cracking/remelting have been elaborated. The first quantification of graphite nucleation rate is provided, it increases exponentially once a critical undercooling is reached, peaks, and then and then declines sharply. It also provides data on the distribution, nucleation and growth of graphite in a high temperature alloy. The results can be directly used to inform existing models, while the experimental methods can be applied to a wide range of other material systems.

Data statement

Due to its large size, the underlying raw data is not shared online, but representative sample data is included in the Figures and supplementary data. The entire datasets are stored at DLS, and are available from the authors on reasonable request.

Acknowledgements

This work would not have been possible without generously funding from Engineering and Physical Sciences Research Council (EPSRC, grant no. EP/I02249X/1) and Research Fund for Coal and Steel (RFCS, grant no. RFSR-PR-10005 DDT). MAA would like to thank Research Complex at Harwell for continuously supporting his research. MAA would also like to acknowledge funding from University Research Program of Ford Motor Company and NERC (NE/M013561/1), a part of this paper was written while MAA was working on those projects. MKB was supported financially by the Strategic Research Center 'REWIND', Danish Research Council for Strategic Research, grant no. 10-093966. The authors would like to thank Diamond Light Source (DLS), UK, especially the remarkable support they received from the I12 beamline staff during the EE12204-1 beam time. The authors would like to thank Dr. Kion Norman from DTU Energy for help with TOF-SIMS analysis.

Appendix A. Supplementary data

Supplementary data related to this article can be found at https://doi.org/10.1016/j.actamat.2018.06.007.

References

[1] E. Martínez, F. Sanz, S. Pellegrini, E. Jiménez, J. Blanco, Life cycle assessment of a multi-megawatt wind turbine, Renew. Energy 34 (2009) 667–673, https://doi.org/10.1016/j.renene.2008.05.020.
[2] D.M. Stefanescu, G. Alonso, P. Larrañaga, R. Suarez, On the stable eutectic solidification of iron-carbon-silicon alloys, Acta Mater. 103 (2016) 103–114, https://doi.org/10.1016/j.actamat.2015.09.043.
[3] E. Moumeni, D.M. Stefanescu, N.S. Tiedje, P. Larrañaga, J.H. Hattel, Investigation on the effect of sulfur and titanium on the microstructure of lamellar graphite iron, Metall. Mater. Trans. A Phys. Metall. Mater. Sci. 44 (2013) 5134–5146, https://doi.org/10.1007/s11661-013-1897-2.
[4] I.J. Polmear, Light Alloys - from Traditional Alloys to Nanocrystals, Elsevier/Butterworth-Heinemann, 2006, https://doi.org/10.1017/CBO9781107415324.004.
[5] M. Avedesian, H. Baker, ASM Handbook: Magnesium and Magnesium Alloys, ASM International, 1999.
[6] J.R. Joseph, R. Davis, ASM International. Handbook Committee., Cast Irons, ASM International, 1996.
[7] 49th Census of World Casting Production Modest Growth in Worldwide Casting Market, Mod. Cast. (2015) 26–31.
[8] L. Collini, G. Nicoletto, R. Konečná, Microstructure and mechanical properties of pearlitic gray cast iron, Mater. Sci. Eng., A 488 (2008) 529–539, https://doi.org/10.1016/j.msea.2007.11.070.
[9] H. Morrogh, Graphite formation in grey cast irons and related alloys, Bcira 5 (1955) 655, https://doi.org/10.1016/j.gde.2011.01.018.Cohesin.
[10] N.S. Tiedje, Solidification, processing and properties of ductile cast iron, Mater. Sci. Technol. 26 (2010) 505–514, https://doi.org/10.1179/026708310X12668415533649.
[11] A. International, J.R. Davis, ASM Speciality Handbook: Cast Irons, ASM International, 1996.
[12] C. Labrecque, M. Gagne, Ductile iron: fifty years of continuous development, Can. Metall. Q. 37 (1998) 343–378.
[13] H.M. Muhmond, On the Inoculation and Graphite Morphologies of Cast Iron, Royal Institute of Technology, Stockholm, Sweden, 2014.
[14] J. Qing, V.L. Richards, D.C. Van Aken, Examination of spheroidal graphite growth and austenite solidification in ductile iron, Metall. Mater. Trans. A Phys. Metall. Mater. Sci. 47 (2016) 6197–6213, https://doi.org/10.1007/s11661-016-3783-1.
[15] K. Theuwissen, J. Lacaze, L. Laffont, Structure of graphite precipitates in cast iron, Carbon N. Y. 96 (2016) 1120–1128, https://doi.org/10.1016/j.carbon.2015.10.066.
[16] P.D. Lee, J.D. Hunt, Hydrogen porosity in directional solidified aluminium-copper alloys:in situ observation, Acta Mater. 45 (1997) 4155–4169, https://doi.org/10.1016/S1359-6454(97)00081-5.
[17] M. Azeem, P. Lee, A. Phillion, S. Karagadde, P. Rockett, R. Atwood, L. Courtois, K. Rahman, D. Dye, Revealing dendritic pattern formation in Ni, Fe and Co alloys using synchrotron tomography, Acta Mater. 128 (2017) 241–248, https://doi.org/10.1016/j.actamat.2017.02.022.
[18] N. Limodin, L. Salvo, M. Suéry, M. DiMichiel, In situ investigation by X-ray tomography of the overall and local microstructural changes occurring during partial remelting of an Al-15.8 wt.% Cu alloy, Acta Mater. 55 (2007) 3177–3191, https://doi.org/10.1016/j.actamat.2007.01.027.
[19] N. Limodin, L. Salvo, E. Boller, M. Suéry, M. Felberbaum, S. Gailliègue, K. Madi, In situ and real-time 3-D microtomography investigation of dendritic solidification in an Al-10 wt.% Cu alloy, Acta Mater. 57 (2009) 2300–2310, https://doi.org/10.1016/j.actamat.2009.01.035.
[20] D.S. Eastwood, P.M. Bayley, H.J. Chang, O.O. Taiwo, J. Vila-Comamala, D.J.L. Brett, C. Rau, P.J. Withers, P.R. Shearing, C.P. Grey, P.D. Lee, Three-dimensional characterization of electrodeposited lithium microstructures using synchrotron X-ray phase contrast imaging, Chem. Commun. 51 (2015) 266–268, https://doi.org/10.1039/C4CC03187C.
[21] K. Yamane, H. Yasuda, A. Sugiyama, T. Nagira, M. Yoshiya, K. Morishita, K. Uesugi, A. Takeuchi, Y. Suzuki, Influence of Mg on solidification of hypereutectic cast iron: X-ray radiography study, Metall. Mater. Trans. A Phys. Metall. Mater. Sci. 46 (2015) 4937–4946, https://doi.org/10.1007/s11661-015-3077-z.
[22] S. Karagadde, L. Yuan, N. Shevchenko, S. Eckert, P.D. Lee, 3-D microstructural model of freckle formation validated using in situ experiments, Acta Mater. 79 (2014) 168–180, https://doi.org/10.1016/j.actamat.2014.07.002.
[23] J.D. Miller, L. Yuan, P.D. Lee, T.M. Pollock, Simulation of diffusion-limited lateral growth of dendrites during solidification via liquid metal cooling, Acta Mater. 69 (2014) 47–59, https://doi.org/10.1016/j.actamat.2014.01.035.
[24] A.J. Clarke, D. Tourret, S.D. Imhoff, P.J. Gibbs, K. Fezzaa, J.C. Cooley, W.K. Lee, A. Deriy, B.M. Patterson, P.A. Papin, K.D. Clarke, R.D. Field, J.L. Smith, X-ray imaging and controlled solidification of Al-Cu alloys toward microstructures by design, Adv. Eng. Mater. 17 (2015) 454–459, https://doi.org/10.1002/adem.201400469.
[25] H.B. Dong, P.D. Lee, Simulation of the columnar-to-equiaxed transition in directionally solidified Al-Cu alloys, Acta Mater. 53 (2005) 659–668, https://doi.org/10.1016/j.actamat.2004.10.019.
[26] M. Zhu, Z. Li, D. An, Q. Zhang, T. Dai, Cellular automaton modeling of microporosity formation during solidification of aluminum alloys, ISIJ Int. 54 (2014) 384–391, https://doi.org/10.2355/isijinternational.54.384.

[27] M. Drakopoulos, T. Connolley, C. Reinhard, R. Atwood, O. Magdysyuk, N. Vo, M. Hart, L. Connor, B. Humphreys, G. Howell, S. Davies, T. Hill, G. Wilkin, U. Pedersen, A. Foster, N. De Maio, M. Basham, F. Yuan, K. Wanelik, I12: the joint engineering, environment and processing (JEEP) beamline at Diamond Light source, J. Synchrotron Radiat. 22 (2015) 828–838, https://doi.org/10.1107/S1600577515003513.
[28] C. Raven, Numerical removal of ring artifacts in microtomography, Rev. Sci. Instrum. 69 (1998) 2978, https://doi.org/10.1063/1.1149043.
[29] D. Paganin, S.C. Mayo, T.E. Gureyev, P.R. Miller, S.W. Wilkins, Simultaneous phase and amplitude extraction from a single defocused image of a homogeneous object, J. Microsc. 206 (2002) 33–40, https://doi.org/10.1046/j.1365-2818.2002.01010.x.
[30] S. Amini, R. Abbaschian, Nucleation and growth kinetics of graphene layers from a molten phase, Carbon N. Y. 51 (2013) 110–123, https://doi.org/10.1016/j.carbon.2012.08.019.
[31] D.M. Stefanescu, Science and Engineering of Casting Solidification, Springer, 2002.
[32] J. Qing, V.L. Richards, D.C. Van Aken, Growth stages and hexagonal-rhombohedral structural arrangements in spheroidal graphite observed in ductile iron, Carbon N. Y. 116 (2017) 456–469, https://doi.org/10.1016/j.carbon.2017.01.063.
[33] D.M. Stefanescu, G. Alonso, P. Larrañaga, E. De La Fuente, R. Suarez, On the crystallization of graphite from liquid iron-carbon-silicon melts, Acta Mater. 107 (2016) 102–126, https://doi.org/10.1016/j.actamat.2016.01.047.
[34] S.-E. Wetterfall, H. Fredriksson, M. Hillert, Solidification process of nodular cast iron, J. Iron Steel Inst 210 (1972) 323–333.
[35] J. Zhou, W. Schmitz, E. Engler, Untersuchung der Gefügebildung von Gußeisen mit Kugelgraphit bei langsamer Erstarrung, Giessereiforschung 39 (1987) 55–70.
[36] S. Karagadde, P.D. Lee, B. Cai, J.L. Fife, M.A. Azeem, K.M. Kareh, C. Puncreobutr, D. Tsivoulas, T. Connolley, R.C. Atwood, Transgranular liquation cracking of grains in the semi-solid state, Nat. Commun. 6 (2015) 8300, https://doi.org/10.1038/ncomms9300.
[37] H.M. Muhmond, H. Fredriksson, Graphite growth morphologies in cast iron, Mater. Sci. Forum 790–791 (2014) 458–463. www.scientific.net/MSF.790-791.458.
[38] E.J. Freise, A. Kelly, Twinning in graphite, Proc. R. Soc. London. Ser. A Math. Phys. Sci. 264 (1961) 269–276, https://doi.org/10.1098/rspa.1961.0198.
[39] G. Lesoult, M. Castro, J. Lacaze, Solidification of spheroidal graphite cast iron - I. Physcial modelling, Acta Metall. 46 (1998) 983–995.
[40] P.D. Lee, J.D. Hunt, Measuring the nucleation of hydrogen porosity during the solidification of aluminium-copper alloys, Scripta Mater. 36 (1997) 399–404, https://doi.org/10.1016/S1359-6462(96)00411-3.
[41] C. Puncreobutr, P.D. Lee, K.M. Kareh, T. Connolley, J.L. Fife, A.B. Phillion, Influence of Fe-rich intermetallics on solidification defects in Al-Si-Cu alloys, Acta Mater. 68 (2014) 42–51, https://doi.org/10.1016/j.actamat.2014.01.007.
[42] W. Oldfield, A quantitative approach to casting solidification: freezing of cast iron, ASM Trans. Q 59 (1966) 945–961.
[43] G. Lesoult, Modelling the solidification of cast iron : state of the art and usefulness, in: G. Ohira, T. Kusakawa, E. Niyama (Eds.), Phys. Metall. Cast Iron IV, Materials Research Society, Tokyo, 1990, pp. 413–422, https://doi.org/10.1081/E-EEE2-120046011.